PCCP

Influence of an Electrified Interface on the Entropy and Energy of Solvation of Methanol Oxidation Intermediates on Platinum(111) under Explicit Solvation

Journal:	*Physical Chemistry Chemical Physics*
Manuscript ID	CP-ART-11-2021-005358.R1
Article Type:	Paper
Date Submitted by the Author:	13-Jan-2022
Complete List of Authors:	Estejab, Ali; Clemson University, Chemical and Biomolecular Engineering García Cárcamo, Ricardo; Clemson University, Chemical and Biomolecular Engineering Getman, Rachel; Clemson University, Chemical and Biomolecular Engineering

Influence of an Electrified Interface on the Entropy and Energy of Solvation of Methanol Oxidation Intermediates on Platinum(111) under Explicit Solvation

Ali Estejab, Ricardo A. García Cárcamo and Rachel B. Getman*

Department of Chemical and Biomolecular Engineering, Clemson University, Clemson, SC 29634-0909

*rgetman@clemson.edu

Abstract

Liquid water and electric fields play significant roles in phenomena occurring at catalytic and electrocatalytic interfaces; however, how their interplay influences interfacial energetics remains uncertain. Electric fields control the orientations of water molecules, which we hypothesized would influence the solvation thermodynamics of surface species. To explore this hypothesis, we used multiscale simulations involving density functional theory and classical molecular dynamics. We computed the energies and entropies of solvation of surface species on Pt(111), specifically, adsorbed CH_3OH, COH, and CO, which are intermediates in the pathway of methanol oxidation, in the presence of electric fields spanning –0.5 to +0.5 V/Å. We found that both the energy and entropy of solvation depend on the strength and direction of the field, with the entropy of solvation being significantly impacted. Both the energy and entropy dependence on the field can be ascribed to water molecule orientations. Specifically, more positive fields orient water molecules so that they can more effectively hydrogen bond with surface species, which strengthens the energies of solvation. However, at more negative fields, competition with the surface species causes interfacial water molecules to reorient, which leads to disorder in the water structure and hence increased entropy.

Keywords: Aqueous interface, Computational catalysis, Density functional theory, Electrochemical interface, Electric field influence on molecular orientation, Explicit water solvent, Free energy of solvation, Molecular dynamics, Multiscale modeling, Solvent structure, Solvation thermodynamics.

1. Introduction

Environmental issues such as toxic gas emissions and global warming have made it urgent to replace fossil fuels with renewable and sustainable energy conversion technologies.[1, 2] Electrochemical energy conversion and storage systems are excellent potential alternatives to fossil fuels in the power and transportation sectors,[3-6] with fuel cells and batteries being developed and applied on growing scales.[7] In particular, fuel cells can be recharged in a few minutes and exhibit long term stability, giving them significant potential for energy conversion applications.[8, 9]

When speaking of fuel cells, the use of hydrogen as the energy carrier often comes to mind. While hydrogen is promising due to its high energy to weight ratio,[9] it exhibits key drawbacks that make it potentially more problematic than helpful. They are: 1) transporting and storing hydrogen is expensive and energy-intensive, and 2) the energy needed to produce hydrogen is likely to be derived from coal or fossil fuels (although sometimes electricity is used to produce hydrogen via water electrolysis).[10] Methanol and ammonia are alternative sources of hydrogen that bypass these challenges;[11-16] however, current electrocatalysts used to oxidize (and create hydrogen from) these compounds are often comprised of platinum,[17-19] which can be prohibitively expensive and prone to poisoning.[20-23] Hence, new materials that are less expensive and more stable under electrocatalytic operating conditions are needed. A grand challenge in catalyst design is to identify such materials; however, a prerequisite step is to understand how current materials function.

Understanding the mechanism of electrocatalytic reactions is significantly challenging. One of the things that makes this problem so challenging is the liquid reaction environment: water molecules at the electrode interface alter the energies and entropies of surface species and impact the thermodynamics and kinetics of reaction steps.[24-27] Thus, explicit description of liquid

molecules at the electrode interface is needed. However, this complicates experimental and computational probes of electrocatalytic chemistry. Specifically, the large density of molecules present in the liquid system (compared to a gas) increases the number of chemical and physical interactions that influence electrocatalytic behavior. Furthermore, it leads to configurational disorder that induces thermodynamic effects that are not present at gas-solid interfaces.[28, 29] The interplay between the electric field and the liquid at the interface additionally induces phenomena that are not present at thermal-catalytic interfaces, even under liquid conditions. Hence, while aqueous electrocatalytic reactions have been studied for decades,[30-33] there remains a large knowledge gap concerning how liquid molecules interact with electrode surfaces. This knowledge gap greatly inhibits understanding of important aqueous electrocatalytic reactions, which impedes the design of improved materials and inhibits the broader expansion of technologies that rely on electrochemical energy conversion and storage.

As a step toward understanding the electrode interface, several researchers have modeled electrocatalytic phenomena in the presence of an electric field under vacuum[34-38] as well as in presence of solvent.[34, 39-49] One key finding is that the energies of surface species depend on the strength and direction of the applied electric field,[35, 41-47, 50, 51] with energies of intermediates in the pathway for methanol oxidation varying by ~ 0.4 eV as the electric field is adjusted from –1.0 to +1.0 V/Å.[35] The aqueous environment also influences the energies of surface species, and this phenomenon is more pronounced when the surface species form hydrogen bonds with liquid water.[28, 52-54] However, understanding the interplay between an applied electric field and solvent effects and how this interplay influences the free energies of surface species remains unknown,[55] in part because of the need to simultaneously apply explicit liquid solvent and an electric field.

In this work, we use our previously developed method of multiscale sampling (MSS),[54] which combines density functional theory (DFT) calculations and classical molecular dynamics (cMD) simulations to investigate the solvation thermodynamics for species in the pathway for methanol oxidation on Pt electrode surfaces under liquid H_2O in the presence of electric fields. Specifically, we compute energies and entropies of solvation of CH_3OH*, COH*, and CO* (* denote that these species are adsorbed to the Pt electrode surface) in the presence of explicit liquid water solvent and applied electric fields spanning from –0.5 V/Å to + 0.5 V/Å. We show how the electric field influences the structure of liquid H_2O at the Pt electrode surface and how these structural effects influence the energies, entropies, and free energies of solvation of CH_3OH*, COH*, and CO*. Specifically, the electric field influences the orientations of the H_2O molecules near the interface,[56] which affects the energy and entropy of solvation but has a more significant influence on the entropy of solvation of these species.

2. Method

2.1. Simulation Supercell

Pt electrodes are modeled using 4 Pt × 4 Pt periodic slabs, constructed by cleaving a (111) surface from the calculated structure of bulk Pt.[57] The resulting supercells are orthorhombic with dimensions of a = 11.22 Å and b = 9.72 Å. Slab thicknesses of three layers are employed (i.e., slab models contain 48 total Pt atoms). We find this choice gives a maximum difference of 0.09 eV in the DFT results when compared with thicker slab models (see Supporting Information Section S4). Surface species are optimized on the topmost Pt layers.

Two water column heights are employed (Figure 1), one shorter and computationally efficient for the DFT calculations (cell #1) and one taller and more realistic for the cMD

simulations (cell #2). The water column heights in cells #1 and #2 are chosen to balance computational efficiency with accurately capturing the first solvation shell of the surface species (most important for calculating solvation *energies*[28]; cell #1) or the full interfacial structure of H_2O (most important for calculating solvation *entropies*[53, 58]; cell #2). Water column heights needed to accurately capture the first solvation shells and full interfacial structures of H_2O are determined using molecular specific gravity analysis in cMD (see Supporting Information Section S3). In this analysis, the average molecular specific gravity (i.e., molecular density of H_2O relative to the molecular density of bulk liquid H_2O) is plotted as a function of distance from the Pt electrode surface (Figure S5) to identify regions of interfacial and bulk liquid H_2O. In the interfacial region, the molecular specific gravity oscillates with respect to distance from the surface due to H_2O molecule layering on the Pt electrode. In contrast, in the bulk region, the molecular specific gravity evens out at 1.

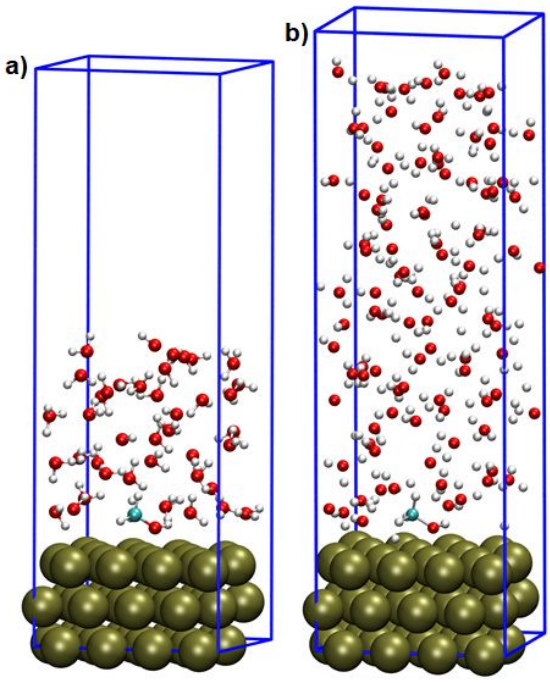

Figure 1. Supercell models used in this work. a) Cell #1 optimized for DFT calculations. b) Cell #2 optimized for cMD calculations. The surface species pictured is CH_3OH*. Pt = gold, C = cyan, O = red, H = white.

In the interfacial region, there is an initial peak which represents the first solvation shell of the surface species (see Figure S5). The water column heights in cell #1 are chosen such that this peak is reasonably well captured when compared to cell #2 while keeping the number of H_2O molecules that need to be added small enough to be computationally tractable for DFT calculations. We find that heights of ~ 12.5 Å, with slight variation depending on the surface species and electric field (see Section 2.3), which correspond to incorporation of 40 H_2O molecules, are sufficient for this purpose. To ensure that 40 H_2O molecules are sufficient for the DFT calculations, we compared DFT results from these cells with results calculated using cells comprising 100 H_2O molecules and found a maximum difference of 0.03 eV (see Supporting Information Section S5). To facilitate calculation in DFT, 14 Å of vacuum space is included above the water columns in cell #1 (Figure 1a) in the DFT calculations (no vacuum space is included in the cMD calculations). We compared this vacuum spacing with cells using 28 Å vacuum space and found a maximum difference of 0.05 eV (see Supporting Information Section S7). A representative snapshot of cell #1 used in DFT calculations is shown in Figure 1a.

Water column heights in cell #2 are chosen such that the H_2O structure comprises interfacial H_2O and at least 10 Å of bulk H_2O (Figure S5), included to ensure the interfacial structure is not influenced by the periodic image of the Pt electrode in the periodic supercell. We find that heights of ~ 29.5 Å, which correspond to incorporation of 100 H_2O molecules, are sufficient for this purpose. A representative snapshot of cell #2 is shown in Figure 1b.

2.2. Free Energy Calculations

Surface species considered in this work are CH_3OH*, COH*, and CO*. These surface species were chosen to compare with our prior work (performed under thermal-catalytic conditions).[53] We

acknowledge that a variety of other intermediates (e.g., CHO*) are possible in catalytic methanol oxidation; however, analysis of the full pathway is reserved for future work.

Interaction energies, entropies, and free energies of solvation for CH_3OH*, COH*, and CO* are calculated using multiscale sampling (MSS), which uses a combination of DFT and cMD:[53]

$$\Delta F_{\mathrm{sol}}^{\mathrm{MSS}} = \Delta E_{\mathrm{int}}^{\mathrm{DFT}} - T\Delta S_{\mathrm{int}}^{\mathrm{cMD}} \quad (1)$$

where $\Delta F_{\mathrm{sol}}^{\mathrm{MSS}}$ is the Helmholtz free energy of solvation, $\Delta E_{\mathrm{int}}^{\mathrm{DFT}}$ is the water-surface species interaction energy calculated with DFT, and $\Delta S_{\mathrm{int}}^{\mathrm{cMD}}$ is the water-surface species interaction entropy calculated with cMD. A flowchart illustrating how these quantities are obtained is provided in Figure S1. The narrative of Figure S1 is as follows. First, DFT is used to obtain the geometry of a surface species on the Pt electrode surface under vacuum. The system is then solvated by introducing H_2O molecules using the MCPliQ code.[54] MCPliQ adds H_2O molecules to the simulation box randomly within user-specified distance criteria. The H_2O molecule positions are then initialized through a sequence of cMD steps (see Section 2.3). H_2O molecule configurations are then produced in the canonical (NVT) ensemble in cMD (see Section 2.3.1).

Configurations of H_2O molecules used to calculate $\Delta E_{\mathrm{int}}^{\mathrm{DFT}}$ are generated in cell #1. $\Delta E_{\mathrm{int}}^{\mathrm{DFT}}$ is then calculated following our prior work [28, 53]:

$$\Delta E_{\mathrm{int}}^{\mathrm{DFT}} = \left\langle \left(E_{\mathrm{Pt+ads}}^{\mathrm{liq}} - E_{\mathrm{Pt+ads}}^{\mathrm{vac}}\right) - \left(E_{\mathrm{Pt}}^{\mathrm{liq}} - E_{\mathrm{Pt}}^{\mathrm{vac}}\right)\right\rangle \quad (2)$$

where $E_{\mathrm{Pt+ads}}^{\mathrm{liq}}$ is the DFT-calculated electronic energy of the Pt electrode surface plus surface species under liquid water, $E_{\mathrm{Pt+ads}}^{\mathrm{vac}}$ is the DFT calculated energy of the Pt electrode surface plus surface species under vacuum, $E_{\mathrm{Pt}}^{\mathrm{liq}}$ is the DFT-calculated energy of the Pt electrode surface under the same liquid structure as for $E_{\mathrm{Pt+ads}}^{\mathrm{liq}}$ but with the surface species removed, $E_{\mathrm{Pt}}^{\mathrm{vac}}$ is the DFT-

calculated energy of the clean Pt electrode surface under vacuum, and the bracket notation indicates the ensemble average.

$T\Delta S_{\text{int}}^{\text{cMD}}$ are calculated using cell #2:[53]

$$T\Delta S_{\text{int}}^{\text{cMD}} = \left(\Delta E_{\text{Pt}+\text{ads}}^{\text{cMD}} - \Delta E_{\text{Pt}}^{\text{cMD}}\right) - \left(\Delta F_{\text{Pt}+\text{ads}}^{\text{cMD}} - \Delta F_{\text{Pt}}^{\text{cMD}}\right) \quad (3)$$

where $\Delta E_{\text{Pt}+\text{ads}}^{\text{cMD}}$ is the average energy of interaction between liquid H_2O molecules and the Pt electrode and surface species, and $\Delta E_{\text{Pt}}^{\text{cMD}}$ is the average energy of interaction between liquid H_2O molecules and the clean Pt electrode (see Section 2.3.1). ΔF^{cMD} are Helmholtz free energies calculated using the method of thermodynamic integration in cMD (see Section 2.3.5).[59, 60] Values of *E* and *F* are calculated relative to the clean Pt electrode in order to isolate the contribution due to the surface species (see Supporting Information Section S10 for an elaborate discussion).

2.3. Classical MD Simulations

cMD calculations are performed with the Large-scale Atomic/Molecular Massively Parallel Simulator (LAMMPS).[61] All cMD simulations are carried out at 300 K. In all cMD simulations, H_2O molecules are allowed to move, while the positions of Pt atoms and surface species atoms are held fixed.[54] All simulations are carried out similar to our prior work.[28, 53, 54] Briefly, H_2O molecules are added to cells #1 and #2 using the MCPliQ code.[54] H_2O molecule positions are then refined in a 0.5 ns cMD simulation performed in the microcanonical (NVE) ensemble to check for energy conservation. Next, a cMD simulation is performed in the isothermal−isobaric (NPT) ensemble for a total of 5 ns to achieve the appropriate water density. In these simulations, the supercell height (*c* dimension) is allowed to vary while the lateral dimensions are held fixed. The average height yields the appropriate water density. Heights for each species at each electric field used in this work are provided in Supporting Information Section S3. Finally, simulations are performed in the NVT ensemble in order to generate configurations of H_2O molecules. Like the

NPT simulations, the NVT simulations are first initialized with a 0.5 ns NVE simulation to check for energy conservation.

2.3.1. Water Molecule Configurations

NVT simulations are performed to produce H_2O molecule configurations for calculating water-surface species interaction energies, water molecule mobilities, and water molecule orientations. A summary of simulation running times and sampling frequencies for each quantity is shown in Table 1. The details are as follows. Simulations used to generate configurations of H_2O molecules for computing $\Delta E_{\text{int}}^{\text{DFT}}$ are carried out for 5 ns, where the first 2 ns are used for system equilibration and the remaining 3 ns are used for the production run (i.e., to generate H_2O molecule configurations for computing the ensemble average). Configurations are sampled every 300 ps (resulting in 10 total configurations), as in prior work.[54] Vacuum space is added to the top of the water column (see Section 2.1), and then the ensemble average is calculated by evaluating Eq. (2). Simulations used for calculating $\Delta E_{\text{int}}^{\text{cMD}}$ are carried out for 30 ns, where the first 2 ns are used for system equilibration and the remaining 28 ns are used for the production run. Configurations are sampled every 1 ps, and the ensemble average is calculated by evaluating the energy of interaction between the H_2O molecules and Pt electrode surface + surface species or the clean Pt electrode in cMD (see Section 2.3.4 for further details). Simulations used for computing H_2O molecule orientations (see Section 2.3.2) are carried out for 30 ns, where the first 2 ns are used for system equilibration and the remaining 28 ns are used for the production run. Configurations are sampled every 10 ps, and the ensemble average is calculated by measuring the angles that the H_2O molecule –OH bonds make with the Pt electrode surface normal (θ_j; see Section 2.3.2). Simulations used for computing H_2O molecule mobilities ($C_{\text{OHb}}(t)$; see Section 2.3.3) are carried out for 5 ns, where the first 2 ns are used for system equilibration and the

remaining 3 ns are used for the production run. The ensemble average is calculated by dividing the production run into 150 ps increments, sampling H_2O molecule configurations every 100 fs within each increment and determining the rotational time correlation function (TCF; see Section 2.3.3). Results presented herein are for one 150 ps increment; however, results from all 150 ps increments are similar.

Table 1. NVT simulation run times and sampling frequencies used to generate H_2O molecule configurations for calculating ΔE_{int}^{DFT}, ΔE_{int}^{cMD}, θ, and $C_{OHb}(t)$.

H_2O molecule configurations for calculating	Supercell model	Total simulation time	Equilibration run duration	Production run duration	Sampling frequency (every…)
$\Delta E_{\mathrm{int}}^{\mathrm{DFT}}$	Cell #1	5 ns	2 ns	3 ns	300 ps
$\Delta E_{\mathrm{int}}^{\mathrm{cMD}}$	Cell #2	30 ns	2 ns	28 ns	1 ps
θ	Cell #2	30 ns	2 ns	28 ns	10 ps
$C_{\mathrm{OHb}}(t)$	Cell #2	5 ns	2 ns	3 ns	100 fs

2.3.2. Water Molecule Orientations

The orientations of H_2O molecules that are hydrogen bonded to surface species are calculated to provide insight into how the H_2O structure is related to solvation thermodynamics. Hydrogen bonds are identified using geometric criteria of O_{H2O}–O_{ads} distances of 3.5 Å or less and O_{ads}–O_{H2O}–H_{H2O} or O_{H2O}–O_{ads}–H_{ads} angles of 30.0° or less.[62, 63] H_2O molecule orientations are tracked by measuring both angles that the H_2O molecule –OH bonds make with the surface normal (θ_1 and θ_2; see **Error! Reference source not found.** for an example).

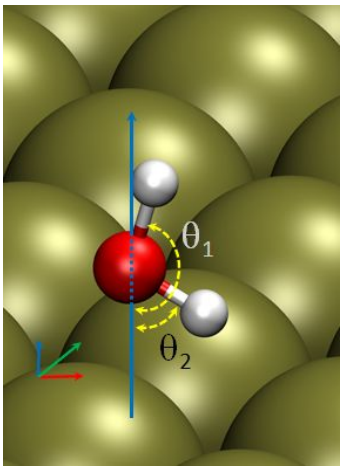

Figure 2. A water molecule and the two angles that its –OH bonds make with the surface normal. Pt = gold, O = red, H = white.

2.3.3. Water Molecule Mobilities

The mobilities of the H_2O molecules that are hydrogen bonded to the surface species are studied using the rotational TCF,[29, 64] as in our prior work.[53] The rotational TCF tracks the orientation of a vector as a function of time t with respect to the original orientation of the vector:

$$C_{\mathrm{OHb}}(t) = \frac{\langle \beta_{ij}(t) \cdot \beta_{ij}(0) \rangle}{\langle \beta_{ij}(0) \cdot \beta_{ij}(0) \rangle} \quad (4)$$

The vectors that we selected were the H_2O molecule –OH bonds. Hence, in Equation (4), $\beta_{ij}(t)$ and $\beta_{ij}(0)$ are the two –OH bonds of the i^{th} hydrogen-bonded H_2O molecule at time t = t and t = 0, respectively (and j is equal to 1 or 2). In our calculations, t = 0 at the formation of a hydrogen bond between a H_2O molecule and a surface species, and we stop computing $C_{\mathrm{OHb}}(t)$ once the hydrogen bond breaks. The rotational TCF is hence an indication of how fast a H_2O molecule rotates away from its initial orientation after forming a hydrogen bond with a surface species.

2.3.4. Force Fields and Parameters

Energies of interaction between H_2O molecules and the Pt electrode and surface species in all cMD simulations are calculated using Lennard-Jones plus Coulomb potentials. Lennard-Jones

parameters for H_2O molecules, Pt atoms, and surface species atoms are taken from the TIP3P,[65-67] UFF,[68] and OPLS-AA[69] force fields, respectively.[53] Pairwise interaction parameters are calculated with geometric mixing rules, except for the intermolecular O-H interactions between water molecules, which are calculated with Lorentz-Berthelot mixing rules.[70, 71] Coulomb charges for Pt atoms and surface species are taken as the partial charges calculated from DFT using the DDEC method,[72] while Coulomb charges for H_2O molecules are taken from the TIP3P force field. All force field parameters and partial charges are listed in Tables S1, S2, S7, S8, and S9 of the Supporting Information.

2.3.5. Thermodynamic Integration Calculations

Thermodynamic integration calculations are carried out to compute Helmholtz free energies of solvation. In this method, a solute (here, the Pt electrode + surface species or the clean Pt electrode) is grown in a solvent (H_2O) over the course of a NVT simulation. The energy of interaction between the solute and solvent over the growth process is integrated to give ΔF^{cMD}. Simulations are run for 45 ns for systems with surface species and 30 ns for the clean Pt electrode surface. In these simulations, the Lennard-Jones and Coulomb parameters are scaled for the surface species, while only the Coulomb charges are scaled for the Pt electrode surface, as in our prior work.[53]

2.4. DFT Calculations

DFT calculations are performed with the Vienna Ab initio Simulation Package (VASP)[73-76] using PAW pseudopotentials,[77, 78] the PBE exchange and correlation functional,[79] and D2 dispersion method,[80] following our prior work.[53] An energy correction for slab-to-slab dipole interactions along the *c* direction is also included.[34, 36, 81] $7 \times 7 \times 1$ Monkhorst – Pack k-point

meshes[82] are used to sample the first Brillouin zones. A sample VASP INCAR file is provided in Section S15 of the Supporting Information.

Geometries, partial charges, and energies of systems with surface species are obtained using partial geometry relaxations. In partial geometry relaxations carried out under vacuum, surface species atoms are allowed to relax, while Pt atoms are held fixed. In partial geometry relaxations carried out under liquid water, the H_2O molecules that are hydrogen bonded to the surface species are allowed to relax, while Pt atoms and the surface species are held fixed. Partial geometry relaxations are considered to be converged when the forces on all of the nonfixed atoms fall below 0.03 eV/Å. Geometries, partial charges, and energies of systems without surface species are calculated using single point calculations. This means that in Equation (2), $E^{\mathrm{liq}}_{\mathrm{Pt}+\mathrm{ads}}$ and $E^{\mathrm{vac}}_{\mathrm{Pt}+\mathrm{ads}}$ are calculated using partial geometry relaxations, while $E^{\mathrm{liq}}_{\mathrm{Pt}}$ and $E^{\mathrm{vac}}_{\mathrm{Pt}}$ are calculated as single points (see Figure S1). The positions of the Pt atoms and H_2O molecules used in the single point calculations are inherited from the parent calculations used to obtain $E^{\mathrm{liq}}_{\mathrm{Pt}+\mathrm{ads}}$, following our prior work.[28] Influence of the relaxation strategy on $\Delta E^{\mathrm{DFT}}_{\mathrm{int}}$ is detailed in Supporting Information Section S6.

2.5. Comparison of MSS With Other Multiscale Methods

Note that the MSS method is sequential in that the surface species structure is generated in DFT, then H_2O configurations are generated in cMD (and used to compute solvation entropies), and then a tractable number of H_2O configurations is sampled and calculated in DFT (and used to compute solvation energies). The rationale for this is that MSS can tractably produce large trajectories of H_2O configurations (needed to compute solvation entropies). However, surface species structures (and hence thermodynamic quantities) cannot be fully precise, since the surface species is held fixed, and hence prevented from responding to H_2O dynamics, during cMD

simulations. A method that would incorporate surface species dynamics is quantum mechanics/molecular mechanics (QM/MM). For example, Heyden developed a state-of-the-art QM/MM method (called explicit solvation model for metal surfaces, or eSMS[83]) to study catalytic chemistry under liquid H_2O.[84, 85] In general, eSMS and MSS arrive at similar conclusions about the influences of liquid H_2O on surface species free energies[52, 84] as well as the ratio of solvation entropy to solvation enthalpy[53, 85] for surface species, indicating that errors due to holding the surface species fixed during cMD simulations should not influence our overall conclusions.

2.6. Inclusion of Electric Fields

Solvation thermodynamics are calculated at electric fields of –0.5, –0.25, 0, +0.25 and +0.5 V/Å, following a prior study.[34, 47] There are multiple approaches for applying electric fields in electrochemical interface simulations. These methods can be divided into two main categories: explicit charge and applied electric field. Explicit charge can be added to the system by adding neutral atoms to the unit cell that subsequently ionize, leaving a charged ion some distance from an oppositely charged metal surface,[45, 46, 86] or by modifying the total number of electrons in the system from its neutral value while compensating with a countercharge.[87, 88] In contrast, in the applied electric field method, presence of charge separation and forces exerted on charged species is represented by application of an external electric field. These two methods for including electric fields have been previously shown to be in good agreement for calculating the free energies of surface species with DFT.[47] In this work, we use the applied electric field method since it can be applied in both the DFT (quantum) and cMD (non-quantum) simulations (since cMD is not equipped to capture charge transfer).

Electric fields are included in all NVT simulations and all DFT simulations. In the NVT simulations, a force equal to the partial charge of each atom times an external electric field (F = q

× E) is applied in the *c* direction using "fix efield" command in LAMMPS. In DFT, an external electric field is applied in the *c* direction using the "EFIELD" command in VASP.

3. Results

Structures of CH_3OH*, COH*, and CO* are shown in Figure 3 along with representative configurations of hydrogen bonded H_2O molecules (determined using geometric criteria). H_2O molecules that hydrogen bond with CH_3OH* and COH* are usually hydrogen bond acceptors (see Figures 3 and S15) that orient "oxygen down" with respect to the Pt electrode surface, i.e., these H_2O molecules point their oxygen atoms toward the Pt electrode surface and their hydrogen atoms into the liquid H_2O structure. This orientation is expected, as it maximizes the number of hydrogen bonds that these H_2O molecules can form (with the surface species and other liquid H_2O molecules).[89]

$\Delta E_{\mathrm{int}}^{\mathrm{DFT}}$ for CH_3OH*, COH*, and CO* are plotted as a function of electric field in Figure 4a. $\Delta E_{\mathrm{int}}^{\mathrm{DFT}}$ for CO* span from +0.07 to –0.13 eV, representing relatively weak interaction with liquid H_2O molecules, in agreement with prior work from our group[28, 54] and others.[90] CH_3OH* and COH* form stronger hydrogen bonds with liquid H_2O molecules via their –OH groups and hence exhibit more negative values of $\Delta E_{\mathrm{int}}^{\mathrm{DFT}}$, with values for CH_3OH* spanning from –0.26 eV to –0.54 eV and values for COH* spanning from –0.51 eV to –0.63 eV. $\Delta E_{\mathrm{int}}^{\mathrm{DFT}}$ for the most part strengthen (get more negative) as the field is adjusted from –0.5 to +0.5 V/Å.

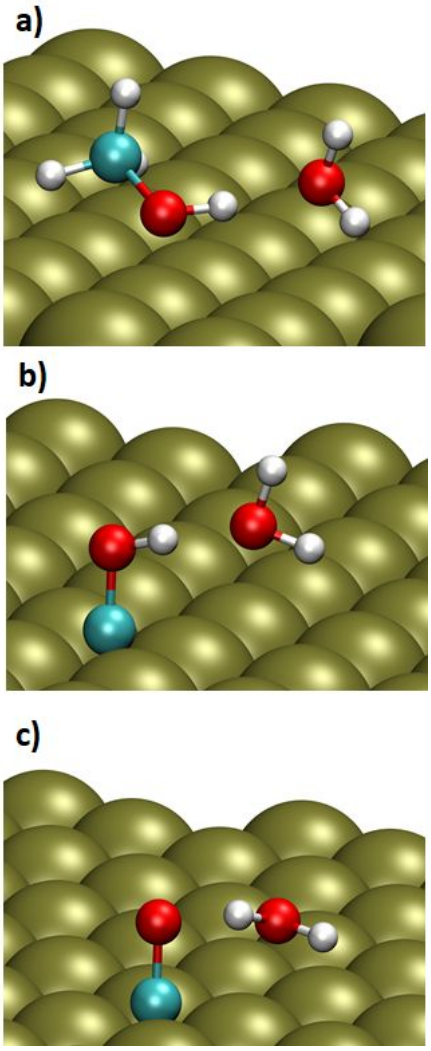

Figure 3. Structures of CH_3OH* (a), COH* (b), and CO* (c) used in this work. A representative hydrogen bonded water molecule (generated in cMD and identified using geometric criteria) is shown for each surface species. Pt = gold, C = cyan, O = red, H = white.

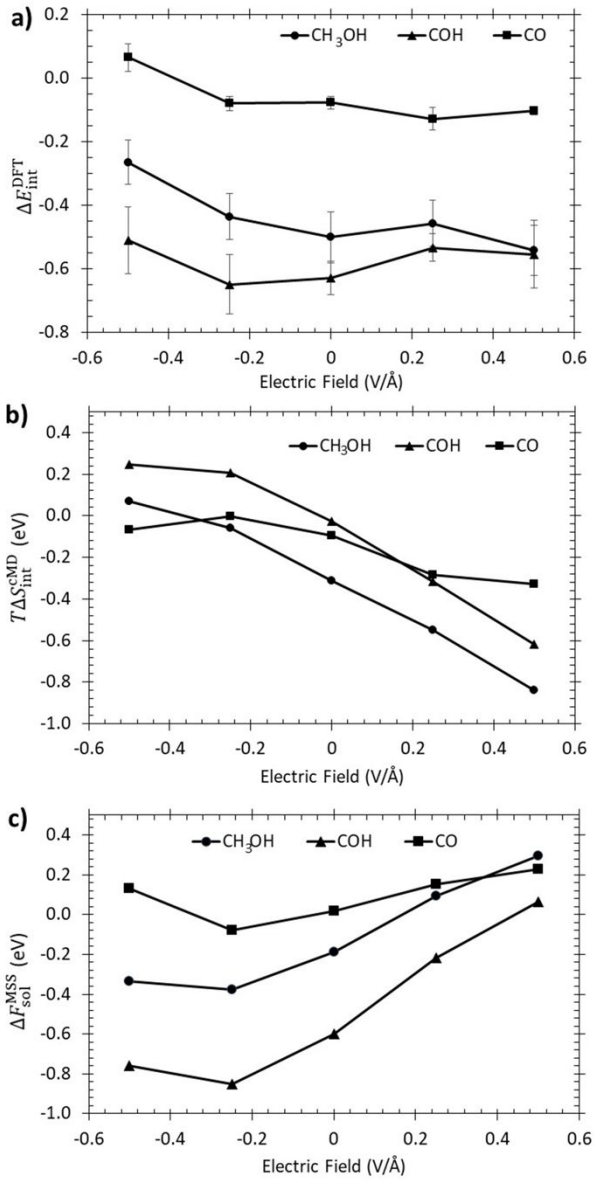

Figure 4. Interaction energies calculated with DFT (a), entropies calculated with cMD (b), and free energies calculated with MSS (c) as functions of electric field for CH_3OH* (circles), COH* (triangles), and CO* (squares). In a) reported values are averages over 10 configurations of water; error bars are the 95% confidence intervals and are a result of the configurational variability of the liquid H_2O structure. *T* used to compute values in b) and c) is equal to 300 K.

$T\Delta S_{\mathrm{int}}^{\mathrm{cMD}}$ are plotted in Figure 4b. Values of $T\Delta S_{\mathrm{int}}^{\mathrm{cMD}}$ for CO* span from 0 to –0.33 eV, while values for CH_3OH* and COH* vary more strongly with electric field. Specifically, $T\Delta S_{\mathrm{int}}^{\mathrm{MD}}$ for CH_3OH* and COH* go from positive at negative electric fields to negative at positive electric

fields, with $T\Delta S_{\mathrm{int}}^{\mathrm{cMD}}$ for CH_3OH* spanning from +0.07 eV at –0.5 V/Å to –0.84 eV at +0.5 V/Å, and $T\Delta S_{\mathrm{int}}^{\mathrm{cMD}}$ for COH* spanning from +0.25 eV at –0.5 V/Å to –0.62 eV at +0.5 V/Å.

$\Delta F_{\mathrm{sol}}^{\mathrm{MSS}}$, obtained by subtracting $T\Delta S_{\mathrm{int}}^{\mathrm{cMD}}$ from $\Delta E_{\mathrm{int}}^{\mathrm{DFT}}$, are plotted in Figure 4c. $\Delta F_{\mathrm{sol}}^{\mathrm{MSS}}$ for CO* span between –0.08 eV and +0.23 eV, while values for CH_3OH* and COH* are more dependent on electric field, with $\Delta F_{\mathrm{sol}}^{\mathrm{MSS}}$ for CH_3OH* spanning from –0.38 eV to +0.30 eV, and $\Delta F_{\mathrm{sol}}^{\mathrm{MSS}}$ for COH* spanning from –0.85 eV to +0.07 eV. That said, $\Delta F_{\mathrm{sol}}^{\mathrm{MSS}}$ for CH_3OH* and COH* are nearly constant below –0.25 V/Å due to nearly identical changes in $\Delta E_{\mathrm{int}}^{\mathrm{DFT}}$ and $T\Delta S_{\mathrm{int}}^{\mathrm{cMD}}$ going from –0.25 to –0.5 V/Å for these surface species.

4. Discussion

Of interest are the dramatic changes in $T\Delta S_{\mathrm{int}}^{\mathrm{cMD}}$ for CH_3OH* and COH* as a function of electric field. That $T\Delta S_{\mathrm{int}}^{\mathrm{cMD}}$ for CO* is not as significantly influenced by electric field as $T\Delta S_{\mathrm{int}}^{\mathrm{cMD}}$ for CH_3OH* and COH* suggests that hydrogen bonding with liquid H_2O molecules contributes to this relationship. We have previously shown that $T\Delta S_{\mathrm{int}}^{\mathrm{cMD}}$ for surface species adsorbed to Pt under thermal-catalytic conditions is related to loss of mobility in the hydrogen bonded H_2O molecules,[53] caused by the strength of the hydrogen bonds, which "lock" the H_2O molecules into place and hence hinder their translational and rotational mobilities. This loss of mobility can lead to an increase in "order" within the H_2O structure; increased order is associated with lower (more negative) entropies. To investigate if this relationship occurs under electric fields, we computed $C_{\mathrm{OHb}}(t)$ for CH_3OH* and COH* as functions of electric field. The results are shown in Figure 5.

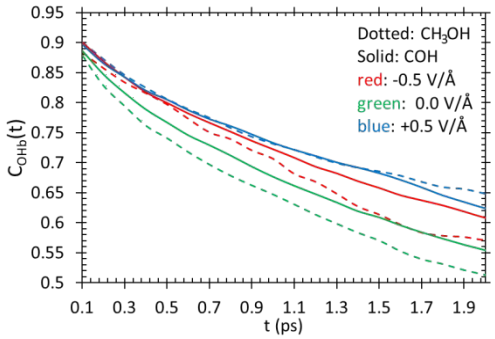

Figure 5. Rotational TCFs calculated with cMD for CH_3OH* (dotted lines) and COH* (solid lines) at electric fields of –0.5 (red lines), 0.0 (green lines), and +0.5 (blue lines) V/Å. $C_{OHb}(t)$ beyond 2 ps shows significant oscillation due to uncertainty caused by the limited number of hydrogen bonds that sustain lifetimes greater than 2 ps; hence, data beyond 2 ps are not shown.

Values of $C_{OHb}(t)$ closer to 1 suggest lower rotational mobility of the hydrogen bonded H_2O molecules. From Figure 5, H_2O molecules at +0.5 V/Å (blue trends) have the lowest mobilities, followed by H_2O molecules at –0.5 V/Å (red trends), followed by H_2O molecules at no electric field (green trends; representing thermal-catalytic conditions). The higher mobilities of the H_2O molecules under thermal-catalytic conditions is because the field influences the H_2O structure (see Refs.[41, 91-93] and Figure 6). As illustrated in Figure 6, at negative fields, H_2O molecules near the Pt electrode surface orient "hydrogen down," whereas at positive fields, H_2O molecules orient "oxygen down". The field hence creates order within the H_2O structure that limits H_2O molecule mobility,[94] which could explain why $C_{OHb}(t)$ at electric fields of –0.5 and +0.5 V/Å are closer to 1 than $C_{OHb}(t)$ under thermal-catalytic conditions. However, two observations contradict H_2O molecule mobility as a dominant phenomenon controlling $T\Delta S_{int}^{cMD}$ over the range of electric fields that we studied. These are that *i*) $T\Delta S_{int}^{cMD}$ in Figure 4b decrease continuously with increasing electric field (i.e., $T\Delta S_{int}^{cMD}|_{-0.5\ V/Å} > T\Delta S_{int}^{cMD}|_{0\ V/Å} > T\Delta S_{int}^{cMD}|_{+0.5\ V/Å}$), whereas $C_{OHb}(t)$ follow the trend $C_{OHb}(t)|_{+0.5\ V/Å} > C_{OHb}(t)|_{-0.5\ V/Å} > C_{OHb}(t)|_{0\ V/Å}$, and *ii*) $C_{OHb}(t)$ for COH* in Figure 5 are in general larger (suggesting lower H_2O molecule mobility) than $C_{OHb}(t)$ for CH_3OH*, whereas

$T\Delta S_{\text{int}}^{\text{cMD}}$ for COH* in Figure 4b are in general more positive (suggesting more disorder) than $T\Delta S_{\text{int}}^{\text{cMD}}$ for CH_3OH*.

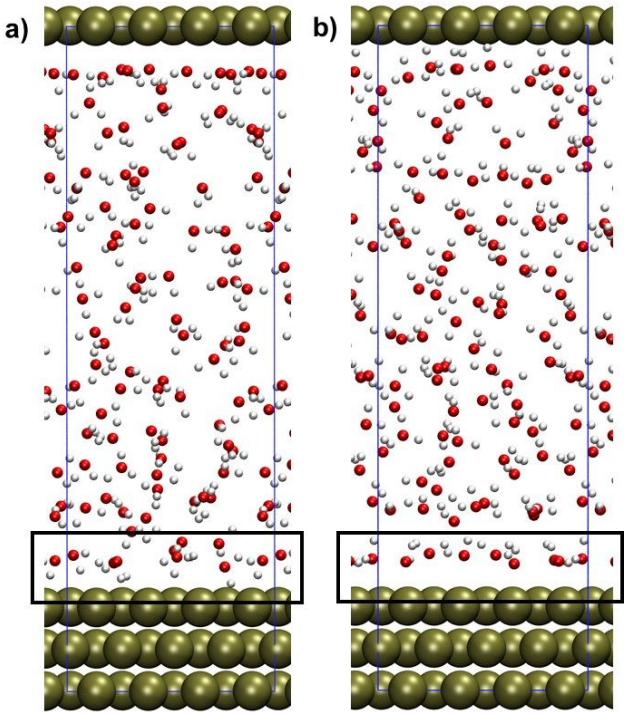

Figure 6. H_2O molecule orientations calculated with cMD at electric fields of a) –0.5 and b) +0.5 V/Å. Black rectangles drawn near the surface are to emphasize how H_2O molecules near negatively charged electrodes (negative electric fields; part a) orient "hydrogen down" whereas H_2O molecules near positively charged electrodes (positive electric fields; part b) orient "oxygen down". Pt = gold, O = red, H = white.

With this in mind, along with the knowledge that electric field influences solvent structure, we postulated that the electric field influence on the water structure could additionally influence $T\Delta S_{\text{int}}^{\text{MD}}$.[41-44] To test this hypothesis, we quantified H_2O molecule orientations by calculating the angles that the H_2O molecule –OH bonds make with the Pt electrode surface (θ_j) at electric fields of –0.5 V/Å, 0 V/Å, and +0.5 V/Å. These angles are plotted in Figure 7 for the clean Pt electrode surface (Figure 7a), CH_3OH* (Figure 7b), and COH* (Figure 7c). Specifically, Figure 7b and 7c plot θ_j

for the H_2O molecules that are hydrogen bonded to CH_3OH* and COH*, respectively, whereas Figure 7a plots θ_j for all H_2O molecules. From Figure 7a, H_2O molecules exhibit near symmetrical distributions of θ_j over the clean Pt electrode at 0 V/Å, with θ_j between 80° and 120° having the largest representation. The distributions are skewed toward lower values of θ_j at –0.5 V/Å, with θ_j between 60° and 80° having the largest representation, and toward larger values of θ_j at +0.5 V/Å, with θ_j between 100° and 120° having the largest representation.

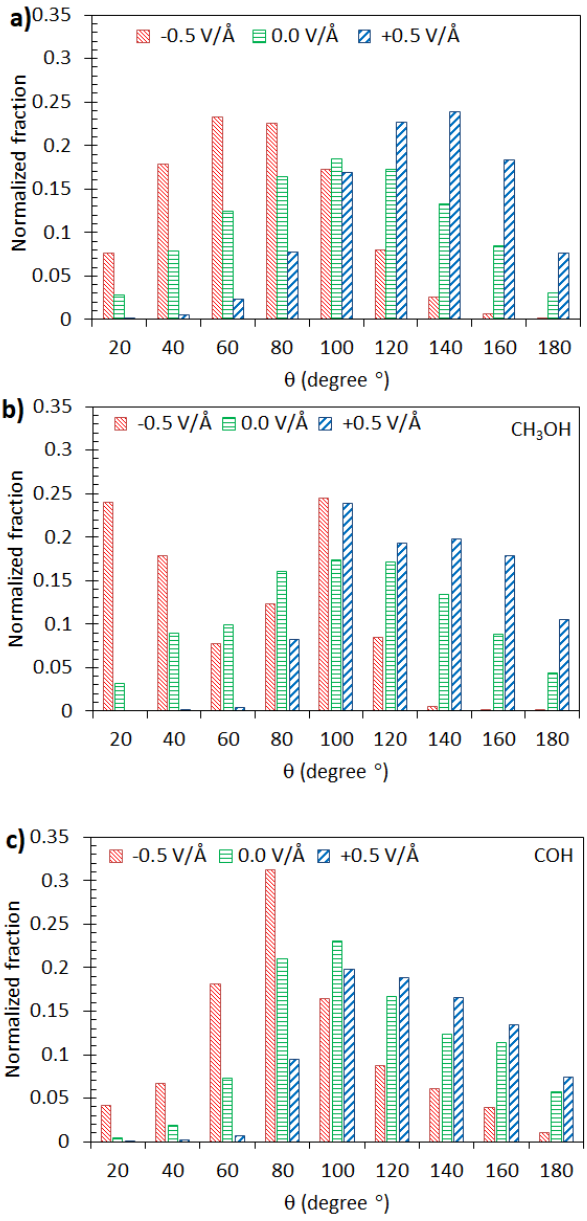

Figure 7. Angles that H_2O molecule –OH bonds make with the Pt electrode surface normal at electric fields of –0.5 (red bars with downward hashes), 0.0 (green bars with horizontal hashes), and +0.5 V/Å (blue bars with upward hashes) in bins of 20°, calculated with cMD. a) All H_2O molecules over the clean Pt electrode. b) H_2O molecules that are hydrogen bonded to CH_3OH*. c) H_2O molecules that are hydrogen bonded to COH*. Normalized fraction refers to normalization by the total number of H_2O molecules in a), the number of H_2O molecules that hydrogen bond to CH_3OH* at +0.5 V/Å in b), and the number of H_2O molecules that hydrogen bond to COH* at 0.0 V/Å in c). In b) and c), the fields were selected to perform the normalization because they had the maximum number of hydrogen bonds for that adsorbate; however, the maximum number of hydrogen bonds is similar at all fields studied.

In general, in the absence of external influences, θ_j for H_2O molecules that hydrogen bond to surface species will tend toward higher values, since this points the –OH groups toward the liquid H_2O structure, hence maximizing opportunities for hydrogen bonding (with surface species and other H_2O molecules).[89] This can be seen in Figures 7b and 7c, where larger values of θ_j are preferred at 0 V/Å. This tendency is amplified at +0.5 V/Å, where there are only a few instances of $\theta_j < 80^o$ (see Figures 7b and 7c). In fact, comparing Figure 7a with Figures 7b and 7c, θ_j for H_2O molecules that are hydrogen bonded to CH_3OH* and COH* approximately follow the same trend as the liquid H_2O structure at 0 V/Å and +0.5 V/Å.

At –0.5 V/Å, there is less agreement between Figure 7a and Figures 7b and 7c. At this field, θ_j for CH_3OH* has large representations at 0^o to 20^o and 80^o to 100^o (looking more like an inverse bell curve). θ_j for COH* are mainly from 60^o to 100^o but span from 0^o and 180^o, which is a greater range of angles than for the clean Pt electrode at this field. This observation suggests that CH_3OH* and COH* have a larger influence on H_2O molecule orientations at negative electric fields than at positive fields (and under thermal-catalytic conditions). A suggestion here is that the competing effects of the surface species and the electric field on H_2O molecule orientations causes disorder, which leads to more positive values of $T\Delta S_{\text{int}}^{\text{cMD}}$. In this scenario, $T\Delta S_{\text{int}}^{\text{cMD}}$ under electric fields is related to surface species inducing disorder in the H_2O structure by competing with the electric field for how to orient H_2O molecules.

Along these lines, the H_2O molecule orientations induced at 0 V/Å and +0.5 V/Å may also explain why $\Delta E_{\text{int}}^{\text{DFT}}$ for CH_3OH* strengthens with increasing field. As oxygen down H_2O orientations enable H_2O molecules to maximize the number of hydrogen bonds that they form, it seems plausible that interactions between the surface species and the liquid H_2O structure are

stronger at these fields. Indeed, analysis of the proportion of hydrogen bonded H_2O molecules that act as hydrogen bond donors increases as the field is made more negative (see Figure S15). Also interesting is that changes in $\Delta E_{\text{int}}^{\text{DFT}}$ with respect to the applied electric field are less significant for COH* than for CH_3OH*. As $\Delta E_{\text{int}}^{\text{DFT}}$ for COH* are quite strong, COH* has a larger control on H_2O molecule orientations at negative fields (as seen in Figure 7c). While this phenomenon causes $T\Delta S_{\text{int}}^{\text{cMD}}$ to depend on the field similar to CH_3OH*, it makes $\Delta E_{\text{int}}^{\text{DFT}}$ less sensitive to the field than for CH_3OH*.

5. Conclusions

In this study, we used a multiscale approach that combines density functional theory with classical molecular dynamics to calculate the energies, entropies, and free energies of solvation for intermediates in the pathway for methanol oxidation on a Pt electrode surface under explicit H_2O solvent and external electric fields. In agreement with prior studies,[35, 41-47, 50, 51] we showed that surface species' energies can be significantly influenced by the strength and direction of an electric field. We further found that solvation free energies depend on the strength and direction of the electric field, and that this is mostly due to the entropy of solvation. Specifically, the entropy of solvation for surface species that hydrogen bond with liquid H_2O molecules goes from positive at an electric field of –0.5 V/Å to negative at a field of +0.5 V/Å. We hypothesized that this was due to disorder in the structure of liquid H_2O at negative fields, which could be caused by a loss in H_2O molecule mobility due to hydrogen bonding or other phenomena occurring in the liquid H_2O structure. Specifically, analysis of the molecular orientations of the H_2O molecules that hydrogen bond with surface species suggests that while all water molecules are experiencing the force exerted by applied electric field, H_2O molecules at the interface can be re-oriented due to

hydrogen bonding with surface species. This competition between the surface species and the electric field and the resulting orientational disorder leads to increases in entropy.

A limitation of the work presented herein is that it does not consider reaction on the Pt electrode surface. For example, H_2O molecules are expected to dissociate on electrode surfaces, forming adlayers of H* and O*,[41] which could influence surface species' free energies. However, modeling – and hence understanding – surface phenomena requires accurate calculation of surface species' free energies, to which solvation contributes significantly. The knowledge presented herein provides insight into the extent that electric fields influence solvation energies and entropies under actual liquid conditions as well as the phenomena that contribute to these quantities. The insights developed herein will be valuable to future studies aimed at determining adlayer coverages as well as reaction energetics on electrode surfaces. Our vision for future work is to use the methods and models developed herein along with the insight garnered to elucidate the relevant surface environments and mechanisms for methanol and ammonia electrocatalytic oxidation, with a long-term goal of learning how to design electrocatalysts for these reactions.

6. Acknowledgments

This research was funded by the National Science Foundation under grant number CBET-1554385. Simulations were performed on the Palmetto Supercomputer Cluster, which is maintained by the Cyberinfrastructure Technology Integration Group at Clemson University. The authors thank Jiarun Zhou (PhD candidate, Clemson University) and Prof. Sapna Sarupria (University of Minnesota) for fruitful discussion on classical molecular dynamics and effect of cell size on solvation as well as Dr. Paul J. Meza-Morales (Clemson University) and Dr. Xiaohong Zhang (formerly at Clemson University and presently at Analytics IQ) for providing preliminary versions of the LAMMPS and VASP scripts as well as for help in the debugging steps. RBG

additionally thanks Prof. Julie Renner (Case Western Reserve University) for helpful discussions about electric fields and water molecule entropy.

Declaration of competing interest

The authors declare no competing interests.

Author contributions using the CRediT model:

Ali Estejab: Conceptualization, Methodology, Validation, Formal analysis, Investigation, Data Curation, Writing – Original Draft, Writing – Review & Editing, Visualization. **Ricardo A. García Cárcamo:** Methodology, Writing – Review & Editing. **Rachel B. Getman:** Conceptualization, Resources, Data Curation, Writing – Review & Editing, Supervision, Project administration, Funding.

References

1. M. Fontecave, *Angewandte Chemie International Edition*, 2011, **50**, 6704-6705.
2. P. C. K. Vesborg and T. F. Jaramillo, *RSC Advances*, 2012, **2**, 7933-7947.
3. P. Yang and J.-M. Tarascon, *Nature Materials*, 2012, **11**, 560-563.
4. F. Díaz-González, A. Sumper, O. Gomis-Bellmunt and R. Villafáfila-Robles, *Renewable and Sustainable Energy Reviews*, 2012, **16**, 2154-2171.
5. S. G. Chalk and J. F. Miller, *Journal of Power Sources*, 2006, **159**, 73-80.
6. M. Armand and J. M. Tarascon, *Nature*, 2008, **451**, 652-657.
7. M. Cheng, L. Sun, G. Buja and L. Song, *Energies*, 2015, **8**.
8. J. M. Ogden and J. Nitsch, *Solar hydrogen*, Island Press, Washington, DC (United States), United States, 1993.
9. Z. P. Cano, D. Banham, S. Ye, A. Hintennach, J. Lu, M. Fowler and Z. Chen, *Nature Energy*, 2018, **3**, 279-289.
10. S. E. Hosseini and M. A. Wahid, *International Journal of Energy Research*, 2020, **44**, 4110-4131.
11. U. B. Demirci, *Journal of Power Sources*, 2007, **169**, 239-246.
12. S. Gunduz, D. J. Deka and U. S. Ozkan, *Journal of Catalysis*, 2020, **387**, 207-216.
13. R. Palkovits, C. von Malotki, M. Baumgarten, K. Müllen, C. Baltes, M. Antonietti, P. Kuhn, J. Weber, A. Thomas and F. Schüth, *ChemSusChem*, 2010, **3**, 277-282.
14. G. G. Botte, *U.S. Patent No. 8,221,610* 2012.
15. A. Estejab and G. G. Botte, *Computational and Theoretical Chemistry*, 2016, **1091**, 31-40.
16. K. Yang, J. Liu and B. Yang, *Journal of Catalysis*, 2021, DOI: https://doi.org/10.1016/j.jcat.2021.10.029.
17. N. A. I. Md Ishak, S. K. Kamarudin, S. N. Timmiati, N. Karim and S. Basri, *International Journal of Energy Research*, 2021, **45**, 7380-7403.
18. A. Estejab and G. G. Botte, *Molecular Catalysis*, 2018, **445**, 279-292.
19. D. A. Daramola and G. G. Botte, *Journal of Colloid and Interface Science*, 2013, **402**, 204-214.
20. A. Estejab, D. A. Daramola and G. G. Botte, *Water Research*, 2015, **77**, 133-145.
21. G. Q. Lu, W. Chrzanowski and A. Wieckowski, *The Journal of Physical Chemistry B*, 2000, **104**, 5566-5572.
22. V. Rosca and M. T. M. Koper, *Physical Chemistry Chemical Physics*, 2006, **8**, 2513-2524.
23. I. Katsounaros, M. C. Figueiredo, F. Calle-Vallejo, H. Li, A. A. Gewirth, N. M. Markovic and M. T. M. Koper, *Journal of Catalysis*, 2018, **359**, 82-91.
24. W. C. Ketchie, M. Murayama and R. J. Davis, *Topics in Catalysis*, 2007, **44**, 307-317.
25. C. Hartnig and E. Spohr, *Chemical Physics*, 2005, **319**, 185-191.
26. Y. Okamoto, O. Sugino, Y. Mochizuki, T. Ikeshoji and Y. Morikawa, *Chemical Physics Letters*, 2003, **377**, 236-242.
27. A. Rendón-Calle, S. Builes and F. Calle-Vallejo, *Applied Catalysis B: Environmental*, 2020, **276**, 119147.
28. C. J. Bodenschatz, S. Sarupria and R. B. Getman, *The Journal of Physical Chemistry C*, 2015, **119**, 13642-13651.

29. X. Zhang, T. E. Sewell, B. Glatz, S. Sarupria and R. B. Getman, *Catalysis Today*, 2017, **285**, 57-64.
30. N. D. Lang and W. Kohn, *Physical Review B*, 1970, **1**, 4555-4568.
31. P. Gies and R. R. Gerhardts, *Physical Review B*, 1986, **33**, 982-989.
32. H. J. Kreuzer, in *Chemistry and Physics of Solid Surfaces VIII*, eds. R. Vanselow and R. Howe, Springer Berlin Heidelberg, Berlin, Heidelberg, 1990, DOI: 10.1007/978-3-642-75762-4_7, pp. 133-158.
33. H. J. Kreuzer, in *Surface Science of Catalysis*, American Chemical Society, 1992, vol. 482, ch. 18, pp. 268-286.
34. K.-Y. Yeh and M. J. Janik, *Journal of Computational Chemistry*, 2011, **32**, 3399-3408.
35. F. Che, S. Ha and J.-S. McEwen, *Applied Catalysis B: Environmental*, 2016, **195**, 77-89.
36. J. Neugebauer and M. Scheffler, *Physical Review B*, 1992, **46**, 16067-16080.
37. S. A. Akhade, N. J. Bernstein, M. R. Esopi, M. J. Regula and M. J. Janik, *Catalysis Today*, 2017, **288**, 63-73.
38. P. Deshlahra, J. Conway, E. E. Wolf and W. F. Schneider, *Langmuir*, 2012, **28**, 8408-8417.
39. S. Sakong and A. Groß, *ACS Catalysis*, 2016, **6**, 5575-5586.
40. S. R. Kelly, C. Kirk, K. Chan and J. K. Nørskov, *The Journal of Physical Chemistry C*, 2020, **124**, 14581-14591.
41. J. Rossmeisl, J. K. Nørskov, C. D. Taylor, M. J. Janik and M. Neurock, *The Journal of Physical Chemistry B*, 2006, **110**, 21833-21839.
42. D. Cao, G. Q. Lu, A. Wieckowski, S. A. Wasileski and M. Neurock, *The Journal of Physical Chemistry B*, 2005, **109**, 11622-11633.
43. S. A. Wasileski and M. J. Janik, *Physical Chemistry Chemical Physics*, 2008, **10**, 3613-3627.
44. J.-S. Filhol and M. Neurock, *Angewandte Chemie International Edition*, 2006, **45**, 402-406.
45. J. Rossmeisl, E. Skúlason, M. E. Björketun, V. Tripkovic and J. K. Nørskov, *Chemical Physics Letters*, 2008, **466**, 68-71.
46. C. D. Taylor, S. A. Wasileski, J.-S. Filhol and M. Neurock, *Physical Review B*, 2006, **73**, 165402.
47. Yeh, K.-Y. , Janik and J. M. , in *Computational Catalysis*, 2014, DOI: 10.1039/9781849734905, pp. P001-266.
48. Y. Wang, X. Qin and M. Shao, *Journal of Catalysis*, 2021, **400**, 62-70.
49. X. Nie, W. Luo, M. J. Janik and A. Asthagiri, *Journal of Catalysis*, 2014, **312**, 108-122.
50. K.-Y. Yeh, N. A. Restaino, M. R. Esopi, J. K. Maranas and M. J. Janik, *Catalysis Today*, 2013, **202**, 20-35.
51. J. A. Santana, J. J. Mateo and Y. Ishikawa, *The Journal of Physical Chemistry C*, 2010, **114**, 4995-5002.
52. C. J. Bodenschatz, T. Xie, X. Zhang and R. B. Getman, *Physical Chemistry Chemical Physics*, 2019, **21**, 9895-9904.
53. X. Zhang, R. S. DeFever, S. Sarupria and R. B. Getman, *Journal of Chemical Information and Modeling*, 2019, **59**, 2190-2198.
54. C. J. Bodenschatz, X. Zhang, T. Xie, J. Arvay, S. Sarupria and R. B. Getman, *JoVE*, 2019, DOI: doi:10.3791/59284, e59284.

55. A. Baz, S. T. Dix, A. Holewinski and S. Linic, *Journal of Catalysis*, 2021, DOI: https://doi.org/10.1016/j.jcat.2021.08.043.
56. F. Che, J. T. Gray, S. Ha and J.-S. McEwen, *Journal of Catalysis*, 2015, **332**, 187-200.
57. T. Xie, C. J. Bodenschatz and R. B. Getman, *Reaction Chemistry & Engineering*, 2019, **4**, 383-392.
58. L. Bellarosa, R. García-Muelas, G. Revilla-López and N. López, *ACS Central Science*, 2016, **2**, 109-116.
59. A. R. Leach, *Molecular Modelling: Principles and Applications*, Longman, 1996.
60. M. R. Shirts and V. S. Pande.
61. S. Plimpton, *Journal of Computational Physics*, 1995, **117**, 1-19.
62. A. Luzar and D. Chandler, *Nature*, 1996, **379**, 55-57.
63. J. Teixeira and M. C. Bellissent-Funel, *Journal of Physics: Condensed Matter*, 1999, **2**, SA105.
64. S. Pal, K. Chakraborty, P. Khatua and S. Bandyopadhyay, *The Journal of Chemical Physics*, 2015, **142**, 055102.
65. A. D. MacKerell, D. Bashford, M. Bellott, R. L. Dunbrack, J. D. Evanseck, M. J. Field, S. Fischer, J. Gao, H. Guo, S. Ha, D. Joseph-McCarthy, L. Kuchnir, K. Kuczera, F. T. K. Lau, C. Mattos, S. Michnick, T. Ngo, D. T. Nguyen, B. Prodhom, W. E. Reiher, B. Roux, M. Schlenkrich, J. C. Smith, R. Stote, J. Straub, M. Watanabe, J. Wiórkiewicz-Kuczera, D. Yin and M. Karplus, *The Journal of Physical Chemistry B*, 1998, **102**, 3586-3616.
66. W. L. Jorgensen, J. Chandrasekhar, J. D. Madura, R. W. Impey and M. L. Klein, *The Journal of Chemical Physics*, 1983, **79**, 926-935.
67. W. L. Jorgensen and C. Jenson, *Journal of Computational Chemistry*, 1998, **19**, 1179-1186.
68. A. K. Rappe, C. J. Casewit, K. S. Colwell, W. A. Goddard and W. M. Skiff, *Journal of the American Chemical Society*, 1992, **114**, 10024-10035.
69. W. L. Jorgensen, D. S. Maxwell and J. Tirado-Rives, *Journal of the American Chemical Society*, 1996, **118**, 11225-11236.
70. H. A. Lorentz, *Annalen der Physik*, 1881, **248**, 127-136.
71. D. Berthelot, *C. r. hebd. séances Acad. Sci.* , 1898, 1703−1855.
72. T. A. Manz and N. G. Limas, *RSC Advances*, 2016, **6**, 47771-47801.
73. G. Kresse and J. Hafner, *Physical Review B*, 1993, **47**, 558-561.
74. G. Kresse and J. Hafner, *Physical Review B*, 1994, **49**, 14251-14269.
75. G. Kresse and J. Furthmüller, *Comput. Mater. Sci.*, 1996, **6**, 15 - 50.
76. G. Kresse and J. Furthmüller, *Physical Review B*, 1996, **54**, 11169-11186.
77. P. E. Blöchl, *Physical Review B*, 1994, **50**, 17953-17979.
78. G. Kresse and D. Joubert, *Physical Review B*, 1999, **59**, 1758-1775.
79. J. P. Perdew, K. Burke and M. Ernzerhof, *Physical Review Letters*, 1996, **77**, 3865-3868.
80. S. Grimme, *Journal of Computational Chemistry*, 2006, **27**, 1787-1799.
81. G. Makov and M. C. Payne, *Physical Review B*, 1995, **51**, 4014-4022.
82. H. J. Monkhorst and J. D. Pack, *Physical Review B*, 1976, **13**, 5188-5192.
83. M. Faheem and A. Heyden, *Journal of Chemical Theory and Computation*, 2014, **10**, 3354-3368.
84. M. Saleheen, M. Zare, M. Faheem and A. Heyden, *The Journal of Physical Chemistry C*, 2019, **123**, 19052-19065.
85. M. Saleheen and A. Heyden, *ACS Catalysis*, 2018, **8**, 2188-2194.

86. E. Skúlason, G. S. Karlberg, J. Rossmeisl, T. Bligaard, J. Greeley, H. Jónsson and J. K. Nørskov, *Physical Chemistry Chemical Physics*, 2007, **9**, 3241-3250.
87. M. Otani and O. Sugino, *Physical Review B*, 2006, **73**, 115407.
88. S. Sakong and A. Groß, *The Journal of Chemical Physics*, 2018, **149**, 084705.
89. M. Maurer and C. Oostenbrink, *Journal of Molecular Recognition*, 2019, **32**, e2810.
90. K. Mathew, R. Sundararaman, K. Letchworth-Weaver, T. A. Arias and R. G. Hennig, *The Journal of Chemical Physics*, 2014, **140**, 084106.
91. G. Gonella, E. H. G. Backus, Y. Nagata, D. J. Bonthuis, P. Loche, A. Schlaich, R. R. Netz, A. Kühnle, I. T. McCrum, M. T. M. Koper, M. Wolf, B. Winter, G. Meijer, R. K. Campen and M. Bonn, *Nature Reviews Chemistry*, 2021, **5**, 466-485.
92. X. Xia, L. Perera, U. Essmann and M. L. Berkowitz, *Surface Science*, 1995, **335**, 401-415.
93. R. P. Hardikar, U. Mondal, F. M. Thakkar, S. Roy and P. Ghosh, *Physical Chemistry Chemical Physics*, 2019, **21**, 24345-24353.
94. H. Ren, L. Zhang, X. Li, Y. Li, W. Wu and H. Li, *Physical Chemistry Chemical Physics*, 2015, **17**, 23460-23467.